Editor's Choice
MICROSCOPY

Microscopy, 2016, 391–399
doi: 10.1093/jmicro/dfw018
Advance Access Publication Date: 21 June 2016

Article

Detection of picometer-order atomic displacements in drift-compensated HAADF-STEM images of gold nanorods

Kohei Aso[1,*], Koji Shigematsu[1], Tomokazu Yamamoto[1], and Syo Matsumura[1,2]

[1]Department of Applied Quantum Physics and Nuclear Engineering, Kyushu University, Motooka 744, Nishi-ku, Fukuoka, Japan, and [2]The Ultramicroscopy Research Center, Kyushu University, Motooka 744, Nishi-ku, Fukuoka, Japan

[*]To whom correspondence should be addressed. E-mail: kaso@nucl.kyushu-u.ac.jp

Received 14 April 2016; Accepted 11 May 2016

Abstract

Cs-corrected atomic resolution scanning transmission electron microscopy under a drift-compensated operation enabled us to acquire high-angle annular dark-field (HAADF) images of entire gold nanorods without distortion induced by specimen drift. The precision in locating the atomic columns was evaluated to be ±5 pm in the images thus obtained, which is comparable to the image pixel size. A high-precision HAADF image of a single-crystalline gold nanorod revealed that the tip portions at both ends tended to undergo outward displacements along the rod axis and inward contraction along the perpendicular direction. A single nanosecond pulse shot of laser light with a wavelength of 1064 nm and an average intensity of 7.3 kJ/m^2 pulse deformed the nanorods into spherical shapes. Simultaneously, the particle interior was completely changed into a multiple twin structure. Substantial displacements of atomic columns on the order of several tens of picometers were confirmed to be localized in the corners of domains at multiple twin junctions. Both the magnitude and direction of displacements were linearly relaxed with increasing distance from a multiple junction.

Key words: nanorods, laser light irradiation, HAADF-STEM, atomic resolution electron microscopy, picometer-order analysis

Introduction

Gold nanorods have been attracting broad interest in various science and engineering fields because of their characteristic optical properties [1–4]. Because of their anisotropic rod shape, gold nanorods generate two light-absorption peaks associated with longitudinal and transverse modes of localized surface plasmon resonance (LSPR) in their optical spectra [5]. The light absorption heats up the nanorods through electron–phonon coupling, sometimes deforming their shape [6,7]. Conventional transmission electron microscopy observations have revealed that gold nanorods change their shape into spheres, Φ-shapes or elongated rods when

irradiated with pulsed laser light [8–11]. Recently, we set up a pulsed laser light illumination system attached to a high-voltage electron microscope (HVEM) and conducted *in situ* high-resolution observations of the deformation of gold nanorods in response to near-infrared laser irradiation [12]. We observed that the first laser pulse effectively rendered the nanorods more spherical, but the effect diminished with additional shots because of the blue shift of the longitudinal LSPR band caused by the shape change. Our *in situ* HVEM observations also revealed that the deformation of nanorods was accompanied by atomic restructuring with the formation of stacking faults as well as twinning in the interior [12].

Cs-corrected scanning transmission electron microscopy (STEM) is widely used to observe atomic structures in various nanomaterials because sub-angstrom atomic resolution is routinely achieved [13–15]. High-angle annular dark-field (HAADF) imaging in Cs-corrected STEM can normally be directly interpreted in terms of atom column positions over a wide range of specimen thickness and the defocus condition, in contrast to Cs-corrected high-resolution transmission electron microscopy (CTEM) imaging [14,15]. HAADF-STEM is advantageous especially to atomic resolution observation of crystalline nanoparticles, because the images are free from the background contrast from the supporting carbon film. However, the serial acquisition of STEM image pixels puts it at a disadvantage compared to the parallel acquisition of CTEM image pixels, because the atom column positions imaged in the former are inevitably influenced by instrumental instabilities, such as specimen drift and probe positioning irregularity. Recent advances in post-processing of STEM images have overcome the instrumental instability issues, thereby enabling researchers to determine atomic positions with picometer-order precision, which is much smaller than the image resolution [16–20]. Kimoto *et al.* achieved 5 pm precision by maximum entropy deconvolution of STEM annular dark-field images overlaid with cross-correlation and revealed that thulium atom columns were slightly shifted toward the oxygen position in a $TmFeO_3$ single crystal [17]. Yankovich *et al.* developed a non-rigid registration technique of an image series to correct both specimen drift and electron beam instability and characterized bond length contractions of surface atoms in platinum and gold nanoparticles with 1–2 pm precision [18,19]. Very recently, Goris *et al.* applied such a high-precision STEM technique to electron tomography to reconstruct the 3D atom configuration in a gold decahedral nanoparticle to exclude outward strains near the surface [20]. The measured local lattice strains were discussed in terms of the structural origin of the catalytic properties of gold nanoparticles [20,21].

In this study, we investigated atomic structures in gold nanorods before and after pulsed laser illumination, taking advantage of drift-compensated processing for HAADF-STEM images to achieve precision on the order of several picometers. In particular, the defected structure formed by laser illumination was characterized quantitatively in detail.

Experimental procedure

The gold nanorods used in this study were produced in a hexadecyltrimethylammonium bromide (CTAB) micellar solution by a photochemical method; the nanorods were approximately 50 nm in length and 10 nm in diameter (products of Dai Nihon Toryo Co. Ltd., Japan). Their optical absorption spectra showed peaks at wavelengths of ~520 and 980 nm [22]. The CTAB micelles were partially removed from the gold nanorods by centrifuging the aqueous solution for 10 min at $2 \times 10^4 g$ (where g is gravitational acceleration). One drop of the solution was dropped onto a Quantifoil™ carbon film of sample supporting mesh, which had been rendered hydrophilic by exposure to Ar ions in a plasma cleaner; the sample was then dried by baking at 373 K for 1 h. Some of the prepared samples were subjected to irradiation with infrared laser pulses in a JEM-1300NEF HVEM equipped with a laser irradiation system [12]. The wavelength of the laser pulses was 1064 nm, and the pulse duration was 6–8 ns. The averaged intensity per pulse was measured to be 7.3 kJ/m^2 by a PIN photodiode placed in the specimen chamber.

HAADF-STEM atomic resolution observations of the gold nanorod samples were carried out using a JEM-ARM200F ACCELARM with a cold field-emission gun operated at an acceleration voltage of 120 kV. The probe semi-angle and the probe current were 18.8 mrad and 15 pA, respectively. The angular detection range of the HAADF detector for the scattered electrons was 70–150 mrad. To suppress the influence of sample drift during STEM operation, the observations were conducted with drift compensation by a customized script for Digital Micrograph™, where a rapidly scanned plural HAADF-STEM series of an area of interest was acquired with a dwell time of 1 μs/pixel in 2048 × 2048 pixels. The thus-obtained images in series were refined into 4096 × 4096 pixels by bicubic interpolation and then overlaid on each other with cross-correlation. The coordinates of each atomic column, $\boldsymbol{r}_{i,j}^{\mathrm{exp}}$, were determined as the pixel position giving intensity peak maxima in the overlaid images after smoothing by Gaussian blur.

To measure local displacements of atomic columns, we prepared averaged reference lattices for individual single-crystalline domains of interest. The reference lattice points $\boldsymbol{r}_{i,j}^{\mathrm{ref}}$ were assumed to be given as follows:

$$\boldsymbol{r}_{i,j}^{\mathrm{ref}} = \boldsymbol{r}_{\mathrm{o}} + i\boldsymbol{a} + j\boldsymbol{b} \tag{1}$$

where $\boldsymbol{r}_{\mathrm{o}}$ is the position of the origin, i and j are index integers, and $\boldsymbol{a}$ and $\boldsymbol{b}$ are primitive lattice vectors. The vectors $\boldsymbol{r}_{\mathrm{o}}$, $\boldsymbol{a}$ and $\boldsymbol{b}$ in Eq. (1) were determined as adjustable parameters by minimizing the residual squared sum of deviations $|\Delta\boldsymbol{r}_{i,j}| = |\boldsymbol{r}_{i,j}^{\mathrm{exp}} - \boldsymbol{r}_{i,j}^{\mathrm{ref}}|$ with $\boldsymbol{r}_{i,j}^{\mathrm{exp}}$ in a domain interior whose positional irregularities from the periodicity were less than the detection limit defined by the image pixel size (8.302 pm).

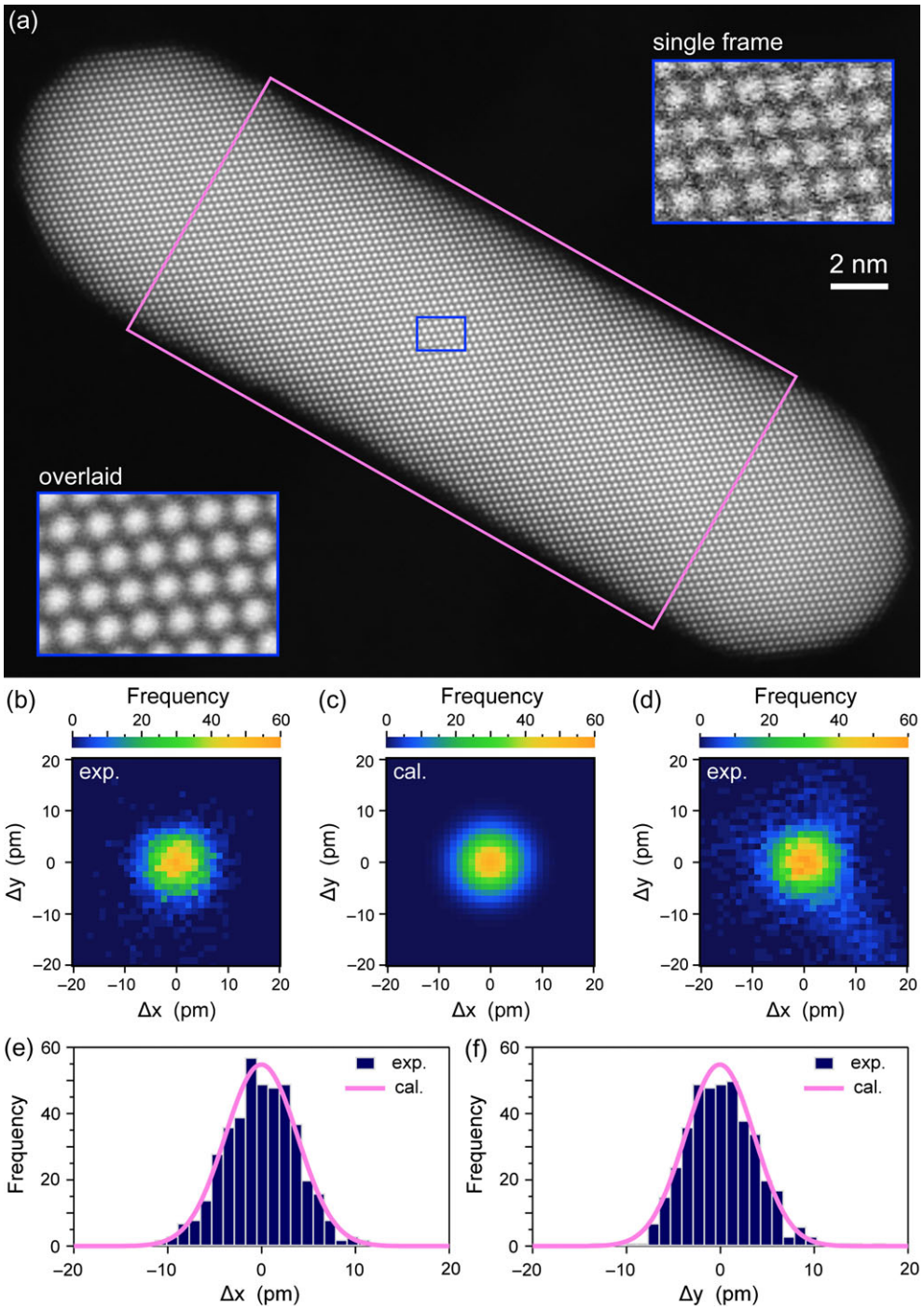

Fig. 1. (a) Drift-compensated atomic resolution HAADF-STEM image of a nanorod. Upper and lower insets are magnified single-frame and overlaid multiple-frame images of the region denoted by a blue rectangle. (b) Histogram of shifts of 3429 atomic columns in the region indicated by a pink rectangle in (a). (c) 2D Gaussian distribution function fitted to the histogram in (b). (d) Histogram of shifts of 5126 columns in the entire nanorod. (e) Distribution of Δx along the axis of $\Delta y = 0$ in (b) and (c). (f) Distribution of Δy along the axis of $\Delta x = 0$ in (b) and (c).

Results and discussion

Figure 1a shows an atomic resolution HAADF-STEM image of a gold nanorod. Here, the incident electrons were illuminated along the [110] zone axis. A perfect regular array of atom columns appears in the nanorod. This nanorod is a single crystal of 34 nm in length and 9 nm in diameter, with its longer axis oriented along [001]. Here, the faceting tendencies of the surfaces of gold nanorods grown with CTAB are confirmed to be {100} for the top and bottom tip ends and {111} for the tip sides. The {110} surfaces in the main middle sides are smooth and almost flat, containing only a few steps of one atomic-layer height. The upper-right and lower-left insets in Fig. 1a are close-up views of a center part of the nanorod in one frame scan and in 29 frames overlaid with cross-correlation, respectively. We are convinced that the drift-compensated operation by overlaying plural images significantly reduces the effect of shot noise and improves the signal-to-noise ratio in the resulting STEM image [16], enabling us to determine the atomic column positions precisely. In addition, it should be noted that this mode of operation is effective in suppressing localized beam heating, which can induce substantial structural changes during observation.

The averaged reference lattice for Fig. 1a was constructed on the basis of the positions of approximately 3000 atomic columns in the middle part of the nanorod. The resultant reference lattice suggests that the interplanar distances of $d_{(002)}$ and $d_{(220)}$ are 199.7 ± 0.5 and 144.3 ± 0.5 pm, respectively, and that the angle between [001] and [110] is 89.6 ± 0.1°. These values are quite satisfactory compared to $d_{(002)}$ = 203 pm and $d_{(220)}$ = 144 pm for 40-nm-diameter gold nanoparticles at 300 K [23]. Thus, the specimen drift has been successfully compensated in Fig. 1a.

Figure 1b gives the distribution of two-dimensional displacements, $\Delta \boldsymbol{r}_{i,j}$, of 3429 atomic columns in the middle part within the pink rectangle in Fig. 1a. The distribution is almost isotropic and mostly ranges within ± 10 pm. Here, the x and y axes are along the horizontal and vertical directions of the scanned image, respectively. The histograms in Fig. 1e and f confirm that Δx and Δy are almost statistically symmetric. We approximated the distribution to a two-dimensional elliptical Gaussian function defined by

$$G(\Delta x,\Delta y) = G_0 \exp\left(-\frac{1}{2(1-\rho^2)}\left[\frac{\Delta x^2}{{\sigma_x}^2} + \frac{\Delta y^2}{{\sigma_y}^2} - 2\rho\frac{\Delta x}{\sigma_x}\frac{\Delta y}{\sigma_y}\right]\right) \quad (2)$$

where G_0 is the maximum peak value, σ_x and σ_y are the standard deviations of Δx and Δy, respectively, and ρ is the correlation coefficient. After the least-squares fitting of the Gaussian function to the distribution, the parameters were determined to be G_0 = 54.8, σ_x = 3.9 pm, σ_y = 3.7 pm, and ρ = 0.0. The Gaussian function thus well reproduces the distribution of displacements, as shown in Fig. 1c, e, and f. Hence, the positions of atomic columns in this image are determined with a precision of ±4 pm corresponding to the standard deviations of σ_x and σ_y. It should be noted that the precision in atomic column positions, which is smaller than the image spatial resolution and the electron beam size, is obtained as the statistical spread of regularity in the periodic array of atomic columns in the image. This precision is considered to approach the achievable limit with the present procedure, being similar to the image pixel size of 8.302 pm. The probe positioning instability of the STEM instrument used in this study was fortunately too small to degrade the precision.

Figure 1d gives the distribution of displacements of 5129 atomic columns in the entire nanorod. The displacements are more dispersed in Fig. 1d than in Fig. 1b, which indicates that several atomic columns in the tip portions at both ends are displaced from their regular positions. We observe that a tail is extended toward the lower right

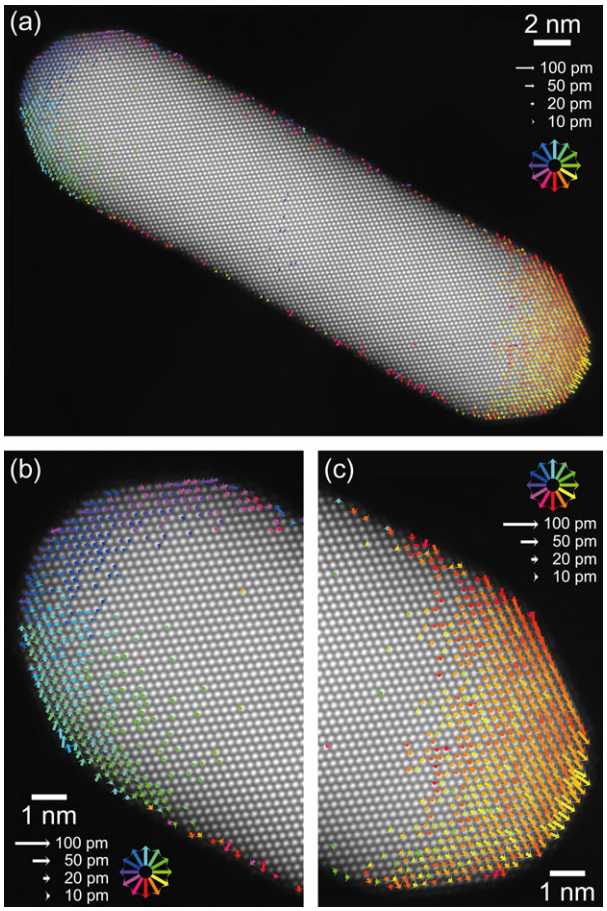

Fig. 2. Atomic displacements larger than 10 pm in the nanorod in Fig. 1. The lengths of arrows are proportional to the displacement magnitudes: (a) the entire rod, (b) the left tip portion and (c) the right tip portion.

direction in Fig. 1d, which indicates collective displacements toward this direction.

In Fig. 2, local displacements larger than 10 pm are shown with arrows that indicate the magnitudes and directions by their lengths and colors, respectively. In the middle of the nanorod, displacements are barely observed within only two or three layers from the side {110} surfaces and the magnitudes are mostly smaller than 20 pm. No systematic tendency of displacement is evident. In contrast, displacements occur extendedly in both tip portions. As shown in Fig. 2b, outward displacements toward the rod axis, or [001] direction, and inward contraction along the perpendicular short axis are observed as a general tendency. Goris *et al.* [24] also observed the outward relaxation along the long axis in the tip parts of a gold nanorod in a uniaxis strain measurement by geometrical phase analysis. The inward contraction of surface atoms is known to be a general feature of precious metal nanoparticles with diameters of approximately 10 nm or smaller [25]. Yankovich *et al.* [19] confirmed the inward contraction shifts of surface atoms in a 5–6 nm gold nanoparticle by high-precision HAADF-STEM imaging. The displacements become more pronounced in the right-side tip in Fig. 2c than that in Fig. 2b. The image in Fig. 2c confirms the tendency of outward displacements along the long axis. In addition, downward displacements appear dominant as a whole in Fig. 2c; these displacements are considered to be responsible for the tail toward the lower right direction in Fig. 1d. The right-side tip portion is likely to be locally bent downward, involving a shear distortion of <0.5%. Such slight distortion is sometimes observed in gold nanorods. Another example is given in Fig. 3a. Here, a perfect array of atomic columns appears in the entire rod, but the contrast appearance of columns is changed locally: it is quite similar in the left-side tip and the middle part, but in the right-side tip portion, it is slightly elongated and the contrast becomes weak. This slight elongation is likely due to the slight inclination of the columns from the zone axis [110]. This nanorod is therefore considered to be slightly bent or twisted.

Figure 3b illustrates an HAADF image obtained after the nanorod in Fig. 3a was exposed to one-shot illumination of a nanosecond laser pulse with $\lambda = 1064$ nm. The viewing orientation in Fig. 3b was almost the same as in Fig. 3a. The outer shape is substantially deformed from its original rod shape to a nearly spherical shape by heating due to laser light absorption. The particle interior is no longer in a single-crystalline state but is divided into several segments with different crystallographic orientations. In the close-up view in Fig. 3c, fine segments are observed in five orientations rotating on a common [110] axis. The segments are separated by single-layer twin boundaries

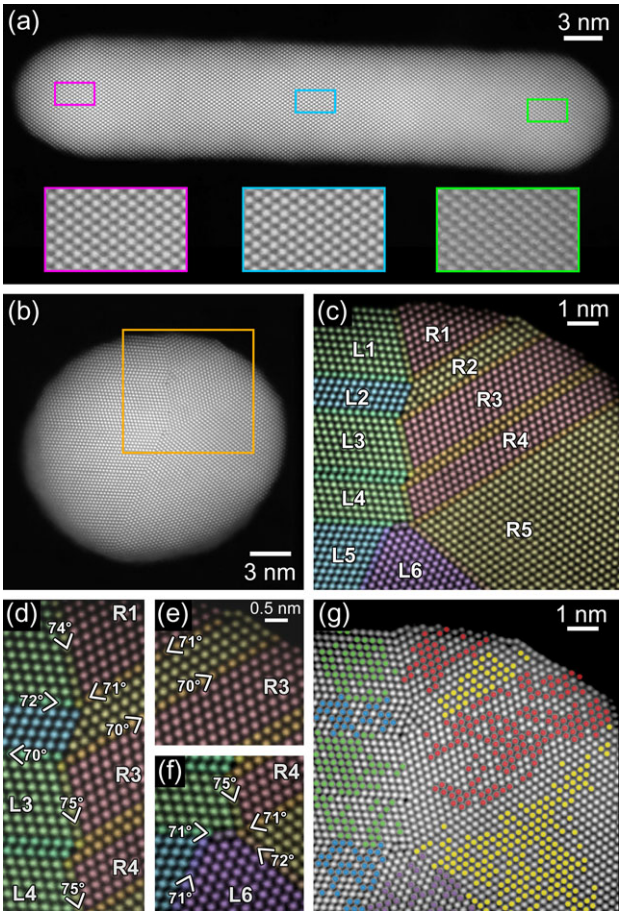

Fig. 3. (a) Atomic resolution HAADF-STEM image of a nanorod before laser illumination. Insets are magnified views of areas indicated by rectangles. (b) Image after one-shot illumination of a nanosecond laser pulse with $\lambda = 1064$ nm. The average intensity is 7.3 kJ/m^2. (c) Enlarged image of the region denoted by the rectangle in (b). The five colors correspond to different crystal orientations of segments. (d)–(f) Further magnified images of regions of interest in image (c). (g) Atomic columns used in the construction of averaged reference lattices for individual segments.

Table 1. Lattice dimensions of averaged reference lattices for segments

Segment	Interplanar distance (pm)		Angle (°)
	$d_{(002)}$	$d_{(220)}$	[001]⊥[110]
L1	199.3 ± 0.8	145.9 ± 0.8	89.3 ± 0.2
L2	202.2 ± 1.1	142.9 ± 0.8	90.5 ± 0.2
L3	199.6 ± 1.0	144.2 ± 0.8	89.2 ± 0.2
L4	199.1 ± 1.1	144.3 ± 0.8	89.2 ± 0.2
L5	201.1 ± 1.0	142.1 ± 0.9	90.4 ± 0.2
L6	199.8 ± 1.0	143.5 ± 1.0	89.3 ± 0.2
R1	200.8 ± 1.2	144.4 ± 0.8	89.2 ± 0.2
R2	202.1 ± 1.1	145.2 ± 1.0	89.1 ± 0.3
R3	204.0 ± 0.8	143.1 ± 0.8	89.4 ± 0.2
R4	201.5 ± 0.8	143.6 ± 0.8	89.6 ± 0.2
R5	199.4 ± 0.9	144.2 ± 0.7	89.3 ± 0.2

with {111} mirror symmetry and double-layered twin or stacking faults. The pronounced surface faceting to {111} or {100} is also recognizable in the upper area of Fig. 3c. Further magnified images around multiple twin junctions and the outer surface are given in Fig. 3d–g. Substantial displacements of atom columns and opening holes are observed at multiple junctions as well as at the surface layer. The averaged reference lattice for the precise analysis of atom positions was constructed for each segment in the same manner as described previously, but using the atom columns marked in Fig. 3h. The lattice parameters of the derived reference lattices are listed in Table 1. These values are similar to those for the aforementioned original nanorod. The image distortion caused by the specimen drift has been successfully compensated again here. The numerical values inserted in Fig. 3d–g represent rotation angles

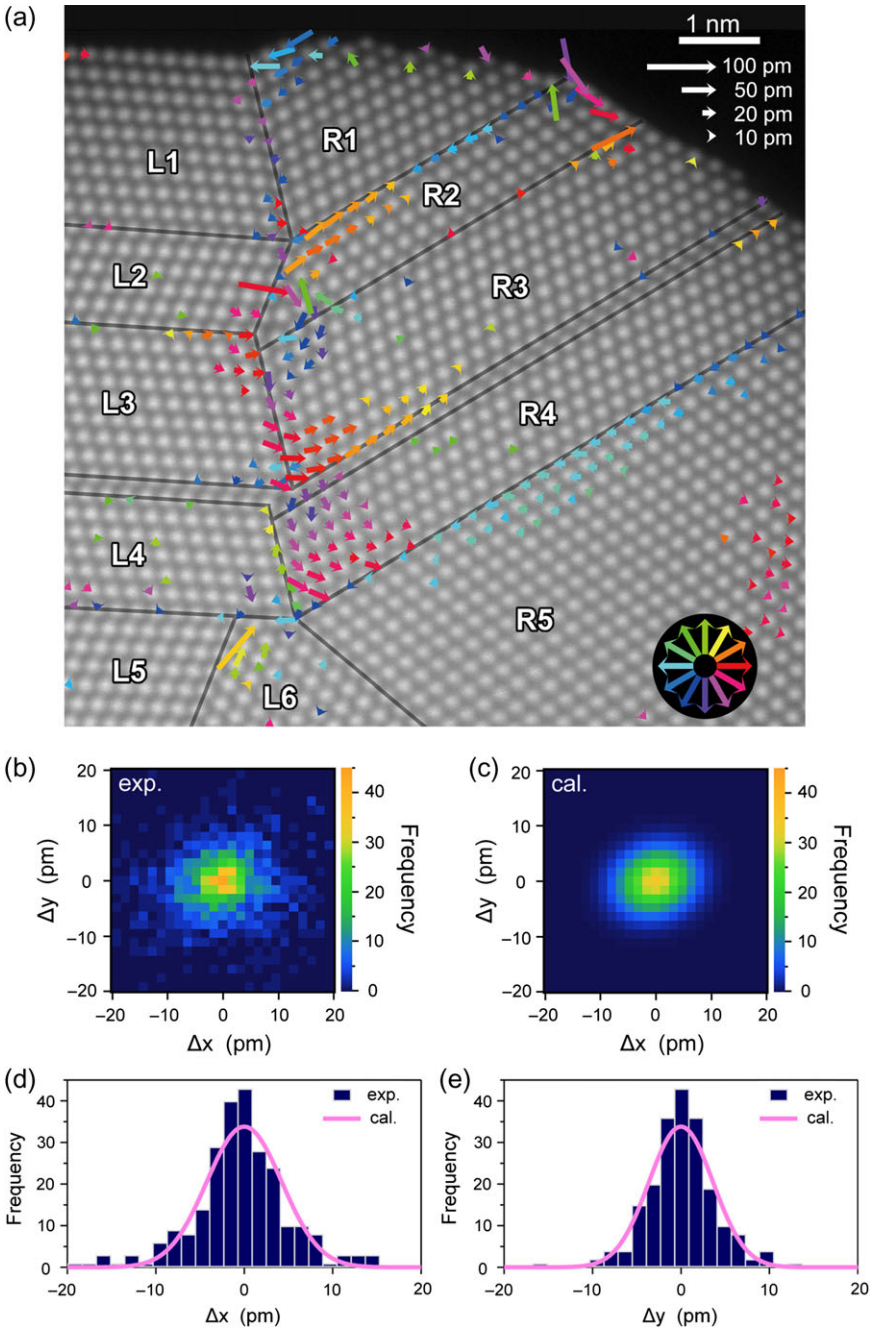

Fig. 4. (a) Local atomic displacements larger than 10 pm in the multiple twinned particle formed by laser illumination. The lengths of arrows are proportional to the displacement magnitudes. (b) Histogram of displacements of 1623 atomic columns in (a). (c) Gaussian distribution function fitted to the histogram in image (b). (d) Distribution of Δx along the axis of $\Delta y = 0$ in (b) and (c). (e) Distribution of Δy along the axis of $\Delta x = 0$ in (b) and (c).

between the reference lattices for individual segments. As is well known, the rotating angle between two {111} twinned orientations is 70.53° for an ideal fcc lattice; a multiple junction of twins therefore results in a solid-angle deficiency or a disclination [26]. As evident in Fig. 3d–f, the rotations become enlarged from the ideal orientation relationship between twinned domains connected with shorter boundaries, specifically between L3 and R3 as well as between L4 and R4. However, the rotation expansion is confined to only a slight increase of one degree or less between domains connected by extended boundaries or between L- or R-grouped segments. This uneven relaxation around the multiple twin junctions is ascribed to the unbalanced force applied to the boundaries.

Local atom displacements in the multiple twinned particle were evaluated by the same procedure previously used to evaluate the virgin nanorod. The results are presented in Fig. 4. Figure 4b gives the 2D histograms of Δx and Δy of 1623 atom columns within the area shown in Fig. 4a. The distribution becomes anisotropic, broadening more along the x direction, in comparison to Fig. 1b, probably as a result of directional displacements caused by defected structures. The 2D histograms of Δx and Δy were approximated by Eq. (2) with $G_0 = 34.0$, $\sigma_x = 4.3$ pm, $\sigma_y = 3.6$ pm, and $\rho = -0.1$, as shown in Fig. 4c–e. The values of σ_x and σ_y are similar to those in Fig. 1c, suggesting that a precision of ± 5 pm would be achieved with respect to the positions of atomic columns in Fig. 4a. Only a limited number of atomic columns would be shifted from their regular positions. Individual displacements larger than 10 pm are represented graphically with arrows in Fig. 4a. Substantial displacements are observed to occur locally around the multiple twin junctions as well as at the surface. The atomic columns at the junctions shift considerably to narrow the center opening holes, influencing the neighborhoods. Displacements toward the lower right occur in the corner areas of Segments R3 and R4. These collective displacements enlarge the rotating angles between the neighboring segments to accommodate the solid-angle deficiency at the multiple twin junctions, which has already been discussed. In

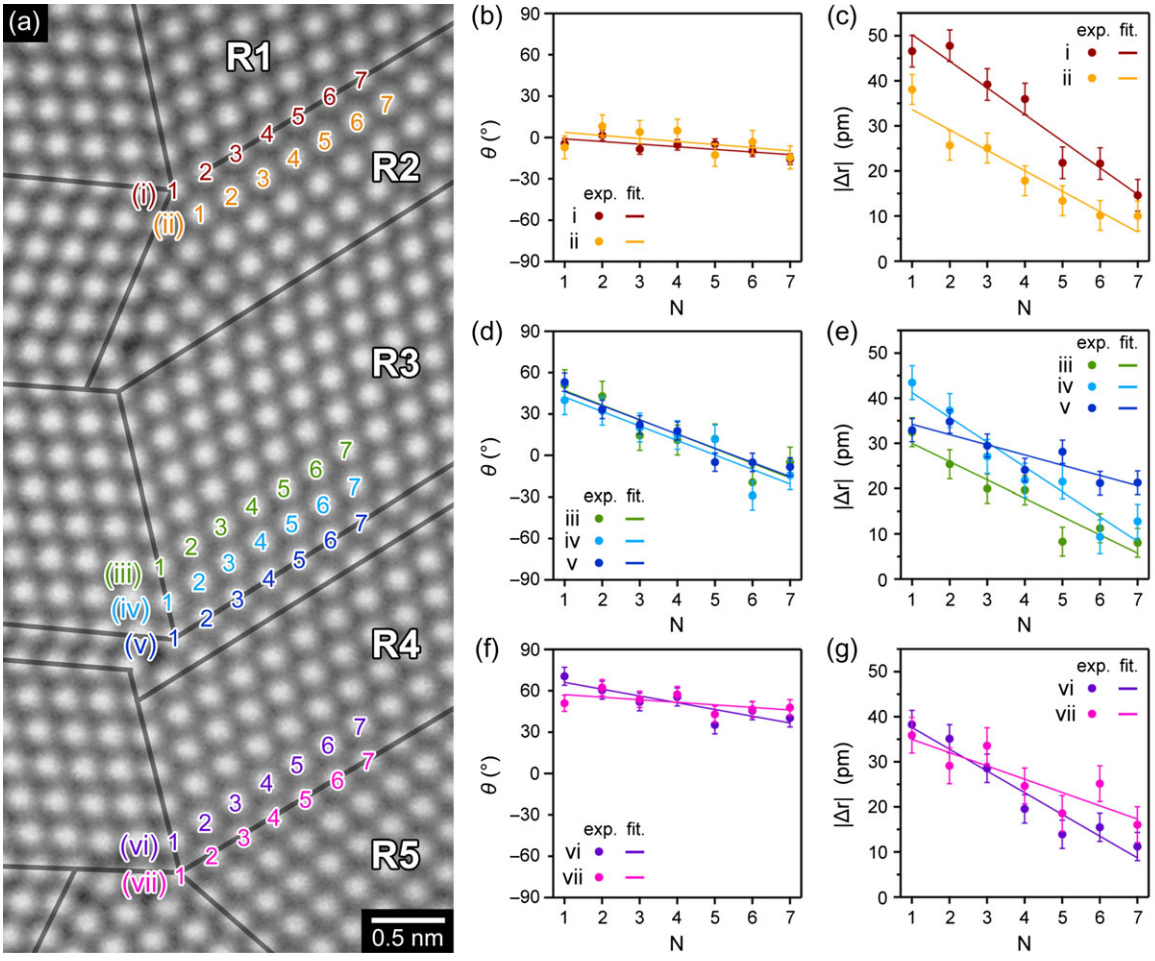

Fig. 5. (a) Atomic rows on and nearby boundaries between Segments R1 and R5. The directions and magnitudes of displacements in (b), (c) Rows (i) and (ii); (d) and (e) Rows (iii)–(v); and (f) and (g) Rows (vi) and (vii). The angles θ of the displacement directions are measured clockwise from the right-hand side direction of the boundary lines.

contrast, the extended twin and doubled twin boundaries on the left side of Fig. 4a are almost free from atomic displacements because the orientation rotations are nearly ideal for the fcc crystal lattice, as indicated in Fig. 3d–f. Using high-precision STEM images, Yankovich *et al.* [19] detected no significant shift in atoms on a twin boundary inserted singly into a gold nanoparticle. Several CTEM studies have identified entirely extended strain due to the solid-angle deficiency in 5-fold symmetric decagonal nanoparticles [21,26]. In contrast to the decagonal nanoparticles, the present multiple twin junctions lose the 5-fold symmetry of the domain segments, thereby localizing deformation in restricted small volumes, as shown in Fig. 4a.

In order to understand the local displacements and their relaxation quantitatively, the direction and magnitude of atomic displacements are given in Fig. 5 as a function of the number of columns, N, from the multiple junctions along the twin or doubled twin boundaries between Segments R1 and R5. The displacements in Rows (i) and (ii) occur toward almost the $\theta = 0°$ direction parallel to the boundary line, and the magnitude decreases linearly with increasing positional number N from the junction, as shown in Fig. 5b and c. As the gradient of the lines gives the local strain, it is revealed that almost constant strain of compression is caused locally along the two atomic rows. In contrast, the displacements in Lines (iii)–(vii) are oriented toward a positive θ of approximately 50° at $N = 1$, and the angle becomes progressively smaller with increasing column number N, as evident in Fig. 5d and f. The magnitude of displacement also decreases linearly with increasing N, as shown in Fig. 5e and g. The linear relaxation of both magnitude and direction characterizes the existence of local compression and shear strain.

Conclusions

In summary, drift-compensated atomic resolution HAADF-STEM images of gold nanorods, obtained by overlaying several images acquired within a short time, enable atomic column positions to be determined with ±5 pm precision, which approaches the image pixel size. The results reveal that a single-crystalline gold nanorod oriented in the [001] direction along its long axis tends to undergo outward displacements toward the rod axis, or the [001] direction, and inward contraction along the perpendicular short axis at both tip end portions. Gold nanorods are deformed into almost spherical shapes and their particle interior changes into a multiple twin structure when the nanorods are exposed to one shot of a laser pulse with a wavelength of 1064 nm and an average intensity of 7.3 kJ/m^2. The extended twin boundaries are almost free from atomic displacements. However, significant displacements on the order of several tens of picometers occur and are localized in the corners of small segments at multiple twin junctions to accommodate the solid-angle deficiency. Both the magnitude and direction of displacements are linearly relaxed with increasing distance from a multiple junction.

Acknowledgements

The authors are indebted to Mr Hiroshi Maeno at the Ultramicroscopy Research Center, Kyushu University, for technical support.

Funding

Grant-in Aid for Scientific Research B (Grant No. 25289221) from JSPS.

References

1. Jain P K, Huang X, El-Sayed I H, El-Sayed M A (2008) Noble metals on the nanoscale: optical and photothermal properties and some applications in imaging, sensing, biology, and medicine. *Acc. Chem. Res.* 41: 1578–1586.
2. Pérez-Juste J, Pastoriza-Santos I, Liz-Marzán L M, Mulvaney P (2005) Gold nanorods: synthesis, characterization and applications. *Coord. Chem. Rev.* 249: 1870–1901.
3. Chen H, Shao L, Li Q, Wang J (2013) Gold nanorods and their plasmonic properties. *Chem. Soc. Rev.* 42: 2679–2724.
4. Huang X, Neretina S, El-Sayed M A (2009) Gold nanorods: from synthesis and properties to biological and biomedical applications. *Adv. Mater.* 21: 4880–4910.
5. Link S, Mohamed M B, El-Sayed M A (1999) Simulation of the optical absorption spectra of gold nanorods as a function of their aspect ratio and the effect of the medium dielectric constant. *J. Phys. Chem. B* 103: 3073–3077.
6. Baffou G, Quidant R, Girard C (2009) Heat generation in plasmonic nanostructures: Influence of morphology. *Appl. Phys. Lett.* 94: 153109.
7. Baffou G, Quidant R (2013) Thermo-plasmonics: using metallic nanostructures as nano-sources of heat. *Laser Photon. Rev.* 7: 171–187.
8. Link S, Burda C, Nikoobakht B, El-Sayed M A (2000) Laser-induced shape changes of colloidal gold nanorods using femtosecond and nanosecond laser pulses. *J. Phys. Chem. B* 104: 6152–6163.
9. Li Y, Jiang Z, Lin X, et al. (2015) Femtosecond laser pulse driven melting in gold nanorod aqueous colloidal suspension: identification of a transition from stretched to exponential kinetics. *Sci. Rep.* 5: 8146.
10. Horiguchi Y, Honda K, Kato Y, Nakashima N, Niidome Y (2008) Photothermal reshaping of gold nanorods depends on the passivating layers of the nanorod surfaces. *Langmuir* 24: 12026–12031.
11. Wang Z L, Mohamed M B, Link S, El-Sayed M A (1999) Crystallographic facets and shapes of gold nanorods of different aspect ratios. *Surf. Sci.* 440: L809–L814.
12. Sumimoto N, Nakao K, Yamamoto T, Yasuda K, Matsumura S, Niidome Y (2014) In situ observation of structural

transformation of gold nanorods under pulsed laser irradiation in an HVEM. *Microscopy* 63: 261–268.
13. Varela M, Lupini A R, van Benthem K, et al. (2005) Materials characterization in the aberration-corrected scanning transmission electron microscope*Annu. Rev. Mater. Res.* 35: 539–569
14. Pennycook S J, Nellist P D (2011) *Scanning Transmission Electron Microscopy*, (Springer, New York).
15. Tanaka N (2014) *Scanning Transmission Electron Microscopy of Nanomaterials*, (Springer, New York).
16. Jones L, Nellist P D (2013) Identifying and correcting scan noise and drift in the scanning transmission electron microscope. *Microsc. Microanal.* 19: 1050–1060.
17. Kimoto K, Asaka T, Yu X, Nagai T, Matsui Y, Ishizuka K (2010) Local crystal structure analysis with several picometer precision using scanning transmission electron microscopy. *Ultramicroscopy* 110: 778–782.
18. Yankovich A B, Berkels B, Dahmen W, et al. (2014) Picometre-precision analysis of scanning transmission electron microscopy images of platinum nanocatalysts. *Nat. Commun.* 5: 4155.
19. Yankovich A B, Berkels B, Dahmen W, Binev P, Voyles P M (2015) High-precision scanning transmission electron microscopy at coarse pixel sampling for reduced electron dose. *Adv. Struct. Chem. Imaging* 1: 2.
20. Goris B, De Beenhouwer J, De Backer A, et al. (2015) Measuring lattice strain in three dimensions through electron microscopy. *Nano Lett.* 15: 6996–7001.
21. Walsh M J, Yoshida K, Kuwabara A, Pay M L, Gai P L, Boyes E D (2012) On the structural origin of the catalytic properties of inherently strained ultrasmall decahedral gold nanoparticles. *Nano Lett.* 12: 2027–2031.
22. Niidome Y, Nishioka K, Kawasaki H, Yamada S (2003) Rapid synthesis of gold nanorods by the combination of chemical reduction and photoirradiation processes; morphological changes depending on the growing processes. *Chem. Commun.* 2376–2377.
23. Solliard C, Flueli M (1985) Surface stress and size effect on the lattice parameter in small particles of gold and platinum. *Surf. Sci.* 156: 487–494.
24. Goris B, Bals S, Van den Broek W, et al. (2012) Atomic-scale determination of surface facets in gold nanorods. *Nat. Mater.* 11: 930–935.
25. Huang W J, Sun R, Tao J, Menard L D, Nuzzo R G, Zuo J M (2008) Coordination-dependent surface atomic contraction in nanocrystals revealed by coherent diffraction. *Nat. Mater.* 7: 308–313.
26. Johnson C L, Snoeck E, Ezcurdia M, et al. (2008) Effects of elastic anisotropy on strain distributions in decahedral gold nanoparticles. *Nat. Mater.* 7: 120–124.